Supplementary Information for

Dual-modal spatiotemporal imaging of ultrafast dynamics in laser-induced periodic surface structures

Qianyi Wei[1], *Jielei Ni*[1], *Yuquan Zhang*[1]*, *Yanan Fu*[1], *Zhangyu Zhou*[1], *Xi Xie*[1], *Yixuan Chen*[1], *Shuoshuo Zhang*[1], *Xiaocong Yuan*[1,2]*, *and Changjun Min*[1]*

[1]Nanophotonics Research Center, Institute of Microscale Optoelectronics & State Key Laboratory of Radio Frequency Heterogeneous Integration, Shenzhen University, Shenzhen 518060, China
[2]Research Center for Humanoid Sensing, Research Institute of Intelligent Sensing, Zhejiang Lab, Hangzhou 311100, China

Correspondence:
Yuquan Zhang(yqzhang@szu.edu.cn)
Xiaocong Yuan(xcyuan@szu.edu.cn)
Changjun Min(cjmin@szu.edu.cn)

Note 1: Experimental calibration of temporal resolution

Experimentally, we adjusted the two arms of the interferometer for the probe light and measured the fringe modulation at various delays, which can be expressed as:

$$K = \frac{I_{max} - I_{min}}{I_{max} + I_{min}} \tag{1}$$

where K represents the fringe visibility, I_{max} denotes the maximum light intensity, and I_{min} indicates the minimum light intensity. We assume that the time profile of the broadened pulse follows a Gaussian distribution, leading to a specific ratio of the pulse width to the width of the fringe visibility waveform of $\sqrt{2}$ [4]. Thus, the pulse width can be measured by assessing the temporal width of the fringe visibility. Since measuring the pulse width directly at the focal plane of the objective lens is challenging, we first measured the pulse width τ_1 in the absence of the objective lens. Subsequently, we determined the pulse width τ_2 after the laser passed through the objective lens, reflected off the sample, and was collected by the objective lens on its return path, which is equivalent to the laser passing through the objective lens twice. By comparing the change in pulse width after passing through the objective lens twice, the second-order dispersion ϕ'' of the objective lens can be obtained, which is mathematically expressed as follows:

$$\phi'' = \frac{1}{2} \cdot \frac{\tau_1 \sqrt{\tau_2^2 - \tau_1^2}}{4\, ln\, 2} \tag{2}$$

Using the method of fringe visibility, we measured the value of τ_1 to be 188.3 fs (**Fig. S1(a)**) and the value of τ_2 to be 393.2 fs (**Fig. S2(b)**). Thus, the second-order dispersion of a single objective lens is determined to be 11708 fs². Consequently, the pulse width on the sample plane is deduced by the second-order dispersion ϕ'' and the pulse width τ_1 before the objective lens,

$$\tau_{sample} = \tau_1 \sqrt{1 + \left(\frac{4ln2 \cdot \phi''}{\tau_1^2}\right)^2} \tag{3}$$

Using **Eq. (3)**, the pulse width of the detection pulse at the sample surface is calculated as 256 fs.

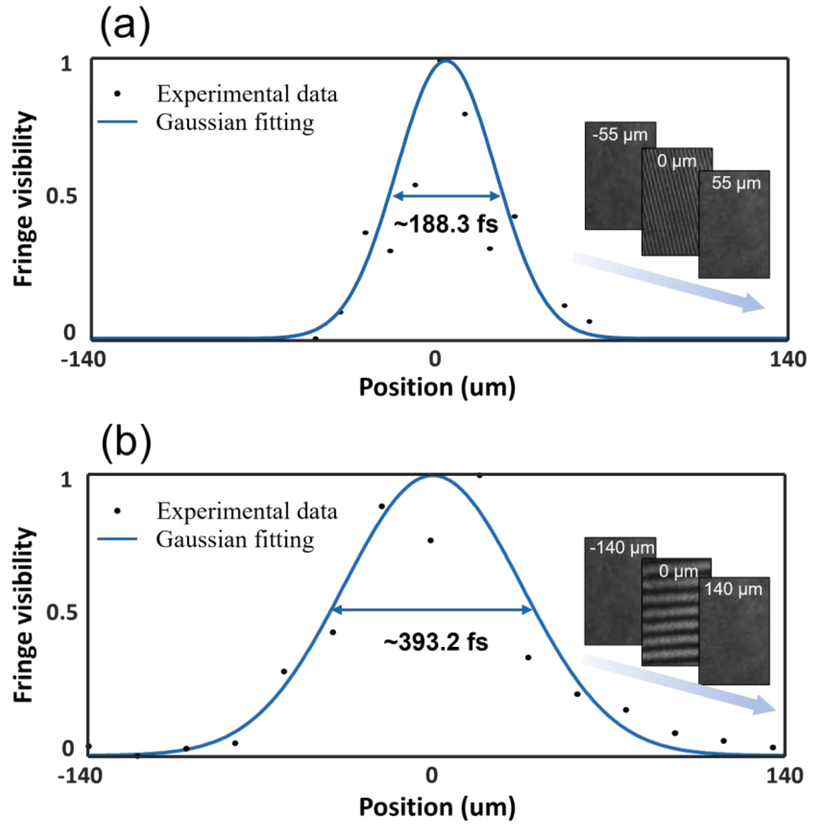

Figure S1. Experimental measurement of temporal resolution in our system. By adjusting the delay between the two arms of the interferometer for the probe pulse, we plotted the fringe modulation K curves at different delay positions and extracted the full width at half maximum (FWHM) of the time profile after Gaussian fitting. (a) The pulse width of the probe light without the objective lens. (b) The pulse width of the probe light after passing through the objective lens twice.

Note 2: Spatial resolution of SPSLM

In SPSLM, to implement triangulation and ensure reconstruction fidelity, the illumination angle of both beams is restricted within the numerical aperture. A typical illumination period of ~478 nm was used in our previous work [3]. To characterize the resolution, the same standard step sample as used in **Fig. 2** is employed to calibrate the SPSLM. The reconstructed depth distribution is shown in **Fig. S2(a)**. By normalizing the one-dimensional height distribution along the white lines, the edge spread function (ESF) (**Fig. S2(b)**) and modulation transfer function (MTF) (**Fig. S2(c)**) are both achieved. Considering the frequency corresponding to a 3% MTF value as the threshold, a spatial resolution of 457 nm is obtained for 3D topography image in SPSLM.

In contrast, our 3D topography modality in this work employs an external interferometric configuration; so, the fringe is controllable by varying the interference angle of the sample beam and reference beam on CCD. This enables the interference fringe periods to approach the diffraction limit and therefore improves the spatial resolution to ~236 nm in **Fig. 2**.

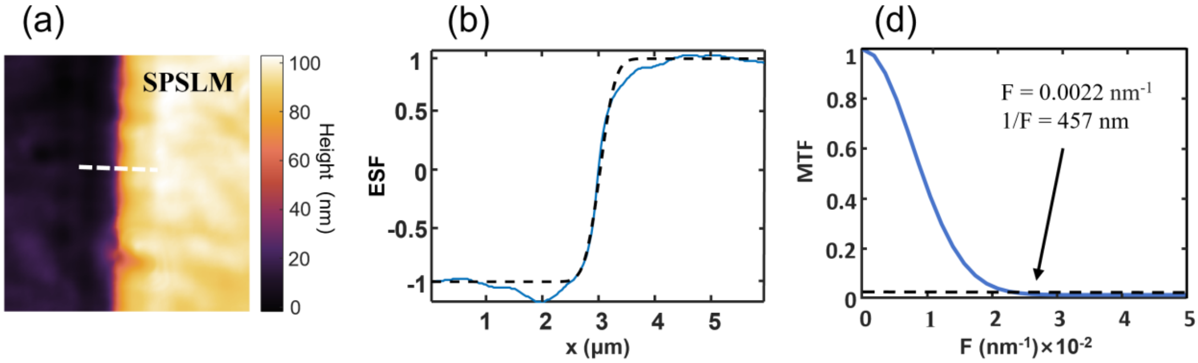

Figure S2. Resolution characterization of SPSLM. (a) The topography of a standard sample (Bruker DektakXT) with height of 83.5±2.8 nm obtained by SPSLM. (b) The normalized height distribution along the white line in (a), and it is fitted by an error function (black dashed line) to obtain the Edge Spread Function (ESF). (c) The modulation transfer function (MTF) result, and it indicates a resolution of 457 nm for a threshold value of 3% (black dashed line).

Note 3: Performance comparison of 3D topography modality and SPSLM

In SPSLM, the probe beam incidents directly toward the DMD to produce diffraction orders. By selecting the +1st and 0-th orders and allowing them to interfere on the sample surface, the interference fringe is formed, as shown in **Fig. S3(a1)**. When the interference pattern obliquely illuminates the sample surface, phase of the fringe is proportional to the surface depth. Depth changes of the surface is obtained by calculating the phase change of reflected fringe at each position using the FTP algorithm. However, it introduces errors in the recovered shape due to stray coherent interference from inter-reflection [1] and shadow effects [2] induced by oblique illumination. To calibrate this error, we use FDTD method to obtain SPSLM imaging of a micro crater structure with diameter of 5 μm and depth of 150 nm on a SiC surface. When the structure is illuminated by two interferential laser beams with normal and 30° incident angles, the reflected light forms distorted interference fringes due to the depth change of the structure, as illustrated in the left panel of **Fig. S3(a2)**. Extracting the phase information from the fringe image enables reconstruction of the crater structure, as shown in the right panel of **Fig. S3(a2)**. The reconstructed structure reveals a tilt height distribution along the incidence direction, with one side exhibiting higher values than the other. Experimental result of an ablated crater using SPSLM with illumination period of 478 nm is displayed in **Fig. S3(a3)**, which demonstrates an inaccurate depth distribution along the projection direction, consistent with the FDTD simulation results. The reconstruction error is enlarged for more oblique illuminations, brings high limitation to the spatial resolution and applications of SPSLM.

The 3D topography modality in this work minimizes these errors caused by shadow effects and stray light through the utilization of a single probe beam that illuminates the sample at near-normal incidence. The reflected beam then interferes with a reference beam which is reflected from a flat surface, as illustrated in **Fig. S3(b1)**. To compare its performance with SPSLM, we simulate the imaging of the same crater structure of **Fig. S3(a2)**. The interference pattern and corresponding reconstruction result are shown in **Fig. S3(b2)**, exhibiting a reconstructed depth distribution with circular symmetry that is highly consistent with the simulated structure. Moreover, the experimental imaging as that in **Fig. S3(a3)** is also conducted. The interference fringe period is set to be 482 nm, close to the illumination period in SPSLM. The reconstructed image, as depicted in the right panel of **Fig. S3(b3)**, demonstrates a spherical crater structure that perfectly corresponds with the profile acquired by AFM (**Fig. S3(b4)**). In comparison of the result obtained by SPSLM (**Figs. S3(a2)** and **S3(a3)**), our 3D topography modality reconstructs the structure with higher fidelity (**Figs. S3(b2)** and **S3(b3)**). These results confirm the superior accuracy of our 3D topography modality in characterizing the depth profiles of surface structures.

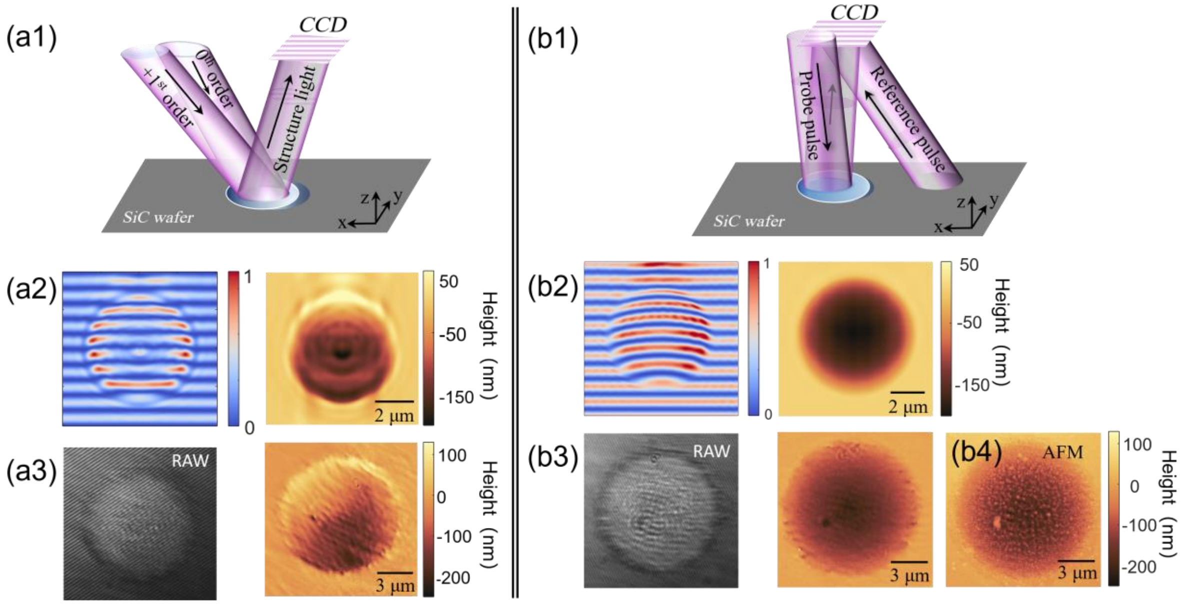

Figure S3. Performance comparison of SPSLM (a) and our 3D topography modality (b). (a2) and (b2) are simulated results of a micro crater structure by FDTD simulation, (a3) and (b3) are the experimental verification. (b4) is the crater topography achieved by AFM.

Note 4: Zero-time point determination in the delay time

To validate the spatiotemporal imaging capability, we adjusted the angle of the pump light to strike the SiC sample surface at a slightly inclined angle, causing a slight time delay at different points on the wavefront reaching the sample surface, as shown in **Figure S4**. The raw images in the first row were captured by a CCD camera at different time delays. The yellow dashed circle in the figure indicates the pump pulse region on the SiC sample, with the onset of the high-density plasma. Here, the initial zero-time point is defined as the moment when the surface modification first becomes visible. **Figure S4** display the results of dual-modal imaging: the second row shows the reflectivity reconstruction results, and the third row shows the height maps calculated by the morphology reconstruction algorithm. It can be seen that, in addition to changes in reflectivity, the surface morphology also changes. After the ultrashort pulse impacts the surface, the reflectivity begins to increase from left to right, spreading to the entire circle region. Subsequently, at 5 ps, the reflectivity at the center starts to decrease, and the morphology shows slight changes. Due to electron collisions, a shallow pit appears on the SiC surface.

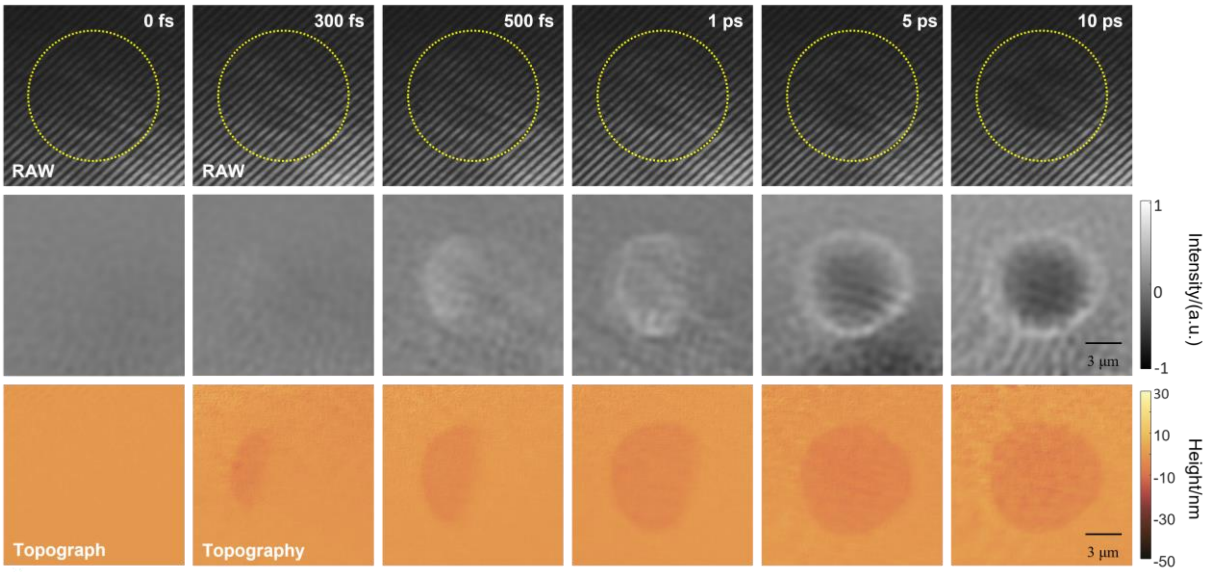

Figure S4. Raw images (first row) acquired near the zero point and reflective images (second row), reconstructed height maps (third row) dual-modal imaging. The time in the figure corresponds to the pump-probe time delay.

Visualization 1. Reflectivity images at different time delay after the irradiation of cross-polarized pulse pairs.

Visualization 2. Topography images at different time delay after the irradiation of cross-polarized pulse pairs.

Visualization 3. Reflectivity images at different time delay after the irradiation of isolated pulses with different polarizations.

Visualization 4. Topography images at different time delay after the irradiation of isolated pulses with different polarizations.

References

[1] Gupta, M. et al. Structured light 3D scanning in the presence of global illumination. *CVPR 2011*, IEEE, 713-720 (2011).

[2] Sun, Z. et al. Discriminative repair approach to remove shadow-induced error for typical digital fringe projection. *Opt. Express* **28**, 26076-26090 (2020).

[3] Xu, J. et al. Imaging ultrafast evolution of subwavelength-sized topography using single-probe structured light microscopy. *Photonics Res.* **10**, 1900-1908 (2022).

[4] Diels, Jean-Claude M., et al. Control and measurement of ultrashort pulse shapes (in amplitude and phase) with femtosecond accuracy. *Appl. Opt.* **24** 1270-1282 (1985).